Spectroscopic study of plasma evolution in runaway nanosecond atmospheric-pressure He discharges

S. Yatom,[1] E. Stambulchik,[2] V. Vekselman,[1] and Ya. E. Krasik[1]
[1]*Department of Physics, Technion, Haifa 32000, Israel*
[2]*Faculty of Physics, Weizmann Institute of Science, Rehovot 76100, Israel*
(Received 22 April 2013; published 30 July 2013; corrected 1 August 2013)

Time- and space-resolved visible-emission spectroscopy measurements are applied to study plasma parameters in nanosecond electrical discharges in He gas at pressure of 10^5 Pa, using a 150 kV, 5 ns duration high-voltage pulse. The plasma evolution during the discharge is investigated by applying line-shape analysis of several He I spectral transitions, with the Stark and opacity effects accounted for. The analysis shows that the discharge plasma is not in equilibrium and that significant electric fields of several kV/cm are present in the plasma during the discharge. Regions of plasma with significantly different electron densities are identified and a qualitative model of the plasma formation and evolution is proposed.

DOI: 10.1103/PhysRevE.88.013107 PACS number(s): 52.80.−s, 52.70.−m, 32.70.Jz, 32.60.+i

I. INTRODUCTION

Nanosecond and subnanosecond discharge in air and helium at elevated pressures $\geqslant 10^5$ Pa is a widely researched subject [1–6]. The common approach for formation of such a discharge without the use of external pre-ionization sources is the application of a high voltage (HV) pulse with amplitude and duration in the ranges 50–300 kV and 150 ps – 20 ns, respectively [1–3]. An important feature is the nonhomogeneity of the electric field distribution in the inter electrode gap, ensured by the form of the cathode. High-energy nonthermal runaway electrons (RAE) are generated during the discharge and are responsible for the pre-ionization of the discharge gap [1]. There are many experimental investigations and analytical and numerical modelings [5,6] related to studies of the formation of the RAE beam and the generation of optical and x-ray emission [7–12] during the discharge. While the emission of RAE from the cathode is a wide consensus [1–3,9], there are also experimental evidence [11] and models [2] for emission of RAE from the ionization front advancing from the cathode to the anode. The latter assumes that the plasma channel behind the ionization front has a sufficient density and temperature in order to carry the cathode potential to the front of the plasma channel propagating towards the anode, and to form at its front a strong electric field sufficient for the generation of the RAE. In order to study parameters of the discharge plasma one can employ a nondisturbing method, such as optical emission spectroscopy, to determine the plasma electron temperature and density. Earlier, spectroscopic studies of repetitive 170 ns duration pulsed discharge have been carried out in atmospheric-pressure N_2 and N_2/H_2O mixture [13]. Another study of repetitive pulsed discharge reports time-averaged values of electron density in He and N_2 gases at the pressure of 10^5 Pa [14]. Also, a pulsed-dc excited atmospheric helium plasma jet was characterized in a study described in Ref [15].

In this work, we present results of time- and space-resolved spectroscopic investigation of the plasma generated during the discharge in He gas at pressure of 10^5 Pa by application of a high-voltage pulse with duration of 5 ns, full width at half maximum (FWHM).

II. EXPERIMENTAL SETUP

In experiments was used an all-solid-state generator based on magnetic compression stages and semiconductor opening switches [9] delivering HV pulses with duration of ∼5 ns FWHM and amplitude of $\leqslant$200 kV to a diode filled with He gas at a pressure $P = 10^5$ Pa, with the cathode-anode (C-A) gap $d_{CA} = 2$ cm [see Fig. 1(a)]. Prior to filling the diode with the gas, the diode was evacuated to a pressure of 0.1 Pa. The discharge voltage and current waveforms [see Fig. 1(b)] were measured using a capacitive voltage divider and self-integrated Rogowski coil, respectively. The cathode was made of a stainless steel blade of 7 mm length and with a width of several μm at its emitting edge. The anode, made of an aluminum disk of 100 mm in diameter, was located at a distance of 2 cm from the cathode. The optical emission from the gas discharge, observed through a Perplex window, was focused using a lens on the entrance slit of a Chromex 500 imaging spectrograph. The lens was placed at an appropriate focal length for each line wavelength. The entrance slit of the spectrograph was set at 100 μm. The instrumental broadening and the focal distance of the lens for each wavelength in the experiment were determined using Hg, Ar, Ar, Ne, and Xe calibration lamps. A fast framing intensified 4QuikE camera (spectral range 350–700 nm) operating with exposure time of 1 ns was coupled to the exit slit of the spectrometer. The CCD matrix of the camera has 300 × 780 elements, with the longer horizontal axis corresponding to the dispersion direction. The 4QuikE camera operation was triggered by the voltage pulse produced by the voltage divider connected to the first magnetic compression stage in the HV generator. The time of the beginning of each camera exposure (t_{shot}) was set as the time delay between the synchronization pulse of the camera and the beginning of the discharge current. A time jitter of ∼1 ns in triggering of the camera allows us to observe different stages of the discharge at different times with respect to the beginning of the discharge current with a 1 ns resolution. The signals from the capacitive voltage divider and the camera synchronization pulse were recorded by a TDS 694C oscilloscope (3 GHz, 10 GS/s), and the image of the spectral lines on the camera output CCD was recorded via the software for 4QuickE.

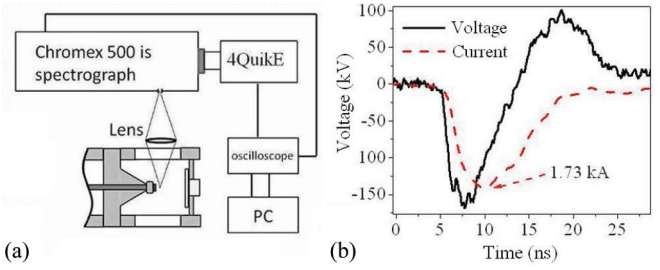

FIG. 1. (Color online) (a) Experimental setup for time- and space-resolved spectroscopy measurements. (b) Voltage and current waveforms obtained in He, with $d_{CA} = 2$ cm.

The coupled system of lens-spectrograph-4QuikE camera was mounted on a single-piece base which was moved with a micrometer, allowing for an observation of different sections of the cathode-anode gap.

III. DATA PROCESSING

In order to achieve reliable results, the most intensive spectral lines in the visible range, with a sufficient He I signal-to-noise ratio observable on the time scale of 1 ns, should be considered. It was found that several spectral lines, namely 388.86, 402.62, 447.15, 492.2, 501.57, 587.56, and 667.82 nm, satisfied these criteria. The emission of these lines was recorded along the whole cathode-edge length of 7 mm. The emission of the spectral lines of He II ions was not detected, not even when the exposure times were extended to >100 ns and with the maximum gain of the framing camera.

The light emission of the discharge plasma in the He gas is characterized by the formation of minor plasma channels along the blade edge and major channels formed at its top or bottom edge or at the both edges, where the most significant electric field enhancement is achieved. Major channels are the ones that advance throughout the C-A gap reaching the anode, while minor channels deviate toward the major channel and overlap with it at some distance from the cathode. Later in a discharge, the major discharge channels mostly appear at the middle of the cathode, apparently due to formation of a significant emission centers at the cathode surface at that location [16]. Therefore, we analyzed the spectral lines emitted from major and minor channel regions separately. The regions of the major discharge channel formation are presented as a broader segment of the spectral line. The spectral line was formed by the light collected from the spatial region of a 2 mm width along the C-A direction. In the experiments, the entrance slit of the spectrograph was imaged at distances of 1 and 5 mm with respect to the cathode emitting edge (d_C), so the light emission was collected from the 0–2 and 4–6 mm segments along the C-A axis, respectively. On average, about 150 generator shots were carried out for acquisition of each spectral line by the 4QuickE camera at the output of the spectrometer for each value of d_C. Each recorded shot was assigned its time delay (t_L) with respect to the earliest shot where the spectral line had distinct shape and intensity sufficient for analyzing. The values t_{shot} for shots with $t_L = 0$ were approximately equal for all spectral lines obtained and analyzed, meaning that all recorded spectral lines appear almost simultaneously in the discharge process. The intensities of the obtained spectral lines diminished to the noise level after 6–9 ns. For the processed shots a vertical segment of ∼1 mm length from major and minor channel regions separately was averaged in the vertical direction to obtain the line shape [see Fig. 2(a)]. The spectral lines were averaged for a 1 ns interval, so that the 0–1 ns time interval, for instance, would be represented by the averaged spectral line profile resulting from 7–10 profiles which belong to $0 < t_L < 1$ ns. In Fig. 2 some of the time intervals were selectively omitted for the sake of clarity.

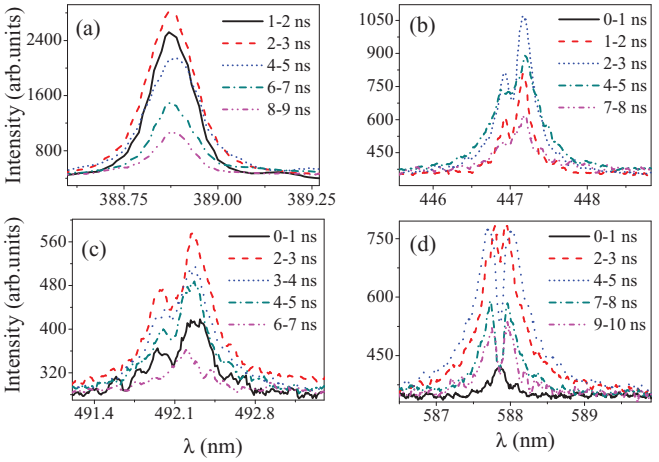

FIG. 2. (Color online) Typical time evolution of several spectral lines at $d_C = 5$ mm, represented by time average of spectral lines over 1 ns intervals. (a) 388.87 nm; (b) 447.15 nm; (c) 492.2 nm; (d) 587.56 nm.

IV. ANALYSIS

A. Preliminary processing of the experimental results

In total, seven He I spectral lines were analyzed: singlet $2s$-$3p$ (388.86 nm), triplet $2s$-$3p$ (501.57 nm), singlet $2p$-$3d$ (667.81 nm), triplet $2p$-$3d$ (587.56 nm), singlet $2p$-$4d$ (492.20 nm), triplet $2p$-$4d$ (447.15 nm), and triplet $2p$-$5d$ (402.62 nm). Because of the high density of the neutral He atoms ($\sim 2 \times 10^{19}\text{cm}^{-3}$), the opacity (self-absorption) affects the line shapes. One can see in Fig. 2(d) that, for the singlet $2p$-$3d$ (667.81 nm) and triplet $2p$-$3d$ (587.56 nm) transitions which are the strongest lines among the observed ones, the opacity is so strong that the self-reversal effect on the line intensity is very pronounced. This effect indicates inhomogeneity of the emissivity and absorption coefficients of these spectral lines along the line of sight in the observed plasma regions. Thus, the use of the emission line widths to determine the plasma density becomes unreliable because of the opacity, yielding only an upper limit of the density. It was suggested [17,18] instead to determine the plasma density using the separation between the allowed (A) and forbidden (F) components of spectral lines 447.15 and 492.20 nm. Due to the mixing of the upper levels by the plasma microfields, the energies of the levels shift depending on the plasma density, while being largely insensitive to the opacity and plasma temperature.

As was previously indicated the 587.56 nm ($2p$-$3d$ triplet) and 667.81 nm ($2p$-$3d$ singlet) spectral lines exhibit strong self-reversal features. However, the absorption profile can be

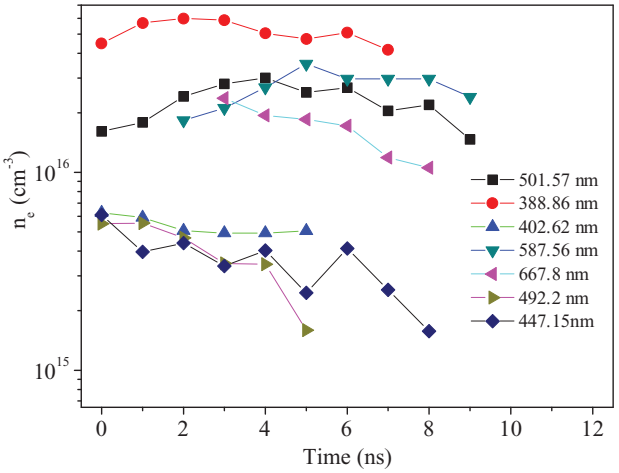

FIG. 3. (Color online) Electron density evolution. Density was calculated using the widths for the 388.86, 501.57, and 402.62 nm lines; using the width of the absorption curve in the line profile for the 587.56 and 667.8 nm lines and using the distance between the forbidden and allowed components for the 492.2 and 447.15 nm lines.

used to calculate the absorbing plasma density by applying the tabulated data in Ref. [19]. Spectral lines 402.62, 388.86, and 501.57 nm do not show strong absorption features, therefore the influence of the opacity on the line profile is uncertain. Thus, these spectral lines together with the data in Ref. [19] were used to calculate the upper limit of electron density. The time evolution of electron density n_e obtained using this analysis is shown in Fig. 3. In the analysis we have also considered the effects of van der Waals (VdW) and resonance broadening on the line widths. The explicit calculations of the broadening due to these mechanisms are shown in Sec. IV B. For calculation of density from the widths of lines 388.86, 501.57, 402.62, 587.56 nm, and 667.81 nm we assumed $T_e = 2$ eV (see Sec. IV B for estimation of electron temperature). One can see that there are two groups of spectral lines representing two different values of electron density which can be related to different factors (plasma nonuniformity and nonequilibrium, existence of external electric field, etc.) which influence the spectral line profile in different ways. To explore these effects a precise analysis of the obtained spectral lines was carried out. This analysis is described in Sec. IV B and it includes opacity effect, Stark broadening, external low-frequency electric field, and collision-radiative (C-R) modeling which also accounts for existence of nonthermal electrons.

B. Spectral lines at $d_C = 5$ mm

Let us start with the opacity effect. With the plasma density determined from the F-A separation, the ratio between the allowed and forbidden component intensities allows us to determine the opacity. Assuming a homogeneous self-absorbing plasma slab, the observed spectrum is given by

$$I(\omega) \sim \tau^{-1}\{1 - \exp[-\tau I_0(\omega)]\}, \tag{1}$$

where $I_0(\omega)$ is line shape calculated in the optically-thin-plasma limit (peak-normalized to unity), and τ is the (peak) line opacity. If the opacity effect is strong, applying Eq. (1) may slightly alter the F-A separation, in which case n_e and τ need to be reevaluated. Typically, one such iteration suffices for convergence.

A criterion for sustainability of the analysis should be a good fit to the entire line shape, within the expected error bars which depend on the signal-to-noise ratio (SNR) of the recorded spectrum. If the best fit of the experimental data is not good enough, the model of the plasma needs to be extended, e.g., assuming plasma not in the thermal equilibrium (i.e., different temperatures of electrons, ions, and neutral radiators), or the existence of macroscopic electric fields. Indeed, in addition to the plasma microfields, the F-A separation is, in general, also sensitive to any other AC or DC electric fields that may be present in plasma. With a sufficiently high SNR level of line-shape data, the effect of such electric fields can be distinguished from that of the plasma microfields [20,21].

Two of the seven spectral lines considered in the present study, namely, the singlet and triplet $2p$-$4d$, are suitable for this approach. The calculations were performed using the computer simulation method described in Ref. [22] with the NIST atomic data [23]. The Stark broadening parameters of the He I lines, including the F-A separation and ratio, have been previously tabulated [24,25]; the agreement between these calculations and our results is within 10% for the plasma parameters considered in the present study.

In addition to the two main line broadening mechanisms, the Stark effect and the opacity, the Doppler effect and broadening due to the neutral perturbers, i.e., the resonance and van der Waals (VdW) broadening, were considered. The resonance broadening FWHM in atomic units is given by ($m_e = \hbar = e = 1$) [26]

$$2\omega_i^r \approx 4\pi N_g \sqrt{\frac{g_g}{g_i}} \frac{f_{gi}}{E_{ig}}, \tag{2}$$

where N_g is the particle density of the He atoms in the ground state, and g_g and g_i are, respectively, the degeneracies of the ground and either the initial or the final state of the line connected to the ground state by a dipole-allowed transition having the absorption oscillator strength f_{gi} and energy E_{ig}. With N_g expressed in cm^{-3} and energies in cm^{-1}, this reads

$$2\omega_i^r \approx 9 \times 10^{-14} N_g \sqrt{\frac{g_g}{g_i}} \frac{f_{gi}}{E_{ig}}. \tag{3}$$

For a weakly ionized plasma, the vast majority of atoms are in the ground state (confirmed by our calculations, see Sec. V), which is a singlet s state. Thus, only transitions from or to a singlet p level are affected by this mechanism. The VdW broadening, expressed in atomic units [26]

$$2\omega_{if}^{\mathrm{VdW}} \approx 2\pi N_g \overline{v^{3/5}} \frac{\left(\overline{R_i^2} - \overline{R_f^2}\right)^{2/5}}{E_p^{4/5}}, \tag{4}$$

where v is the thermal perturber velocity in the center-of-mass frame, E_p is the its excitation energy, and R_i and R_f are the radii vectors of the radiator in states i and f, respectively. The bars over $v^{3/5}$ and R^2 stand for averaging over the thermal velocity distribution and the atomic states, respectively. The

value of $\overline{R^2}$ is approximately evaluated as [27]

$$\overline{R^2} = \frac{n_*^2}{2}[5n_*^2 + 1 - 3l(l+1)]. \quad (5)$$

Here, the effective principal quantum number n_* is $1/\sqrt{2I_i}$, where I_i is the ionization energy of state i, and l is its orbital momentum. With energies in cm^{-1}, the temperature of the neutral gas T_n in eV, and R in units of the Bohr radius, Eq. (4) can be rewritten as

$$2\omega_{if}^{\mathrm{VdW}} \approx 2\times 10^{-16} N_g \left(\frac{T_n}{\mu}\right)^{3/10} \frac{\left(\overline{R_i^2} - \overline{R_f^2}\right)^{2/5}}{E_p^{4/5}}, \quad (6)$$

where μ is the reduced mass (2 for He). Due to the low plasma ionization degree ($\sim 10^{-3}$, see below) and short time scale of the emission ($\lesssim$10 ns), the neutral atoms remain practically at room temperature. This can be shown by assuming the heating is mainly due to the collisional energy loss of the plasma electrons. Indeed, the electron-ion thermal relaxation rate in atomic units is [22]

$$\nu_{ei} = \frac{8\sqrt{2\pi} Z_i^2 n_i \ln\Lambda}{3 m_i T_e^{3/2}}, \quad (7)$$

amounting, for $n_e = n_i = 2\times 10^{16}$ cm^{-3} and $T_e = 2$ eV, to $\nu_{ei} \approx 3.1\times 10^7$ s^{-1}. Here m_i is the ion mass, n_i is the ion density, and $\ln\Lambda$ is the Coulomb logarithm of the electron-ion collisions. The electron-neutral relaxation rate in atomic units is

$$\nu_{en} = 2\sigma_{en} n_n T_e^{1/2}/m_i, \quad (8)$$

where σ_{en} is the electron-neutral collisional cross section. Assuming for the latter $\sigma_{en} = \pi R_{\mathrm{VdW}}^2$ where the He I van der Waals radius $R_{\mathrm{VdW}} \approx 1.4\times 10^{-8}$cm [28], we obtain for the same physical conditions $\nu_{en} \approx 2\times 10^8$ s^{-1}. Therefore, the total thermal relaxation rate from electrons to heavy particles is approximately 2.3×10^8 s^{-1}. In other words, during the entire discharge time of 10 ns, at most $2.3\times\frac{3}{2}T_e = 6.9$ eV per electron can be transferred to neutrals.[1] However, since the amount of neutrals exceeds that of electrons by three orders of magnitude, the thermal energy of each He atom is increased only by 6.9 meV, corresponding to heating by about 50 K. Therefore, for the Doppler and VdW broadening effects, $T_n = 0.03$ eV was assumed.

The results are presented in Table I. As seen, the Doppler broadening is negligible for the conditions of this study. For the analysis, the calculated Stark line shapes were convoluted with the total Lorentzian due to the resonance and VdW broadening effects, then the opacity was accounted for [Eq. (1)], followed by convolution with the Gaussian due to the instrumental broadening.

Ions may gain additional energy by accelerating in the low-frequency electric fields present in the discharge plasma. Fields of the order of 10–20 kV/cm (see below) result, on the scale of the ion mean free path $\approx 10^{-5}$ cm, in an energy gain of about 0.1–0.2 eV. (Here we assumed a He^+-He charge-exchange process with a cross section of $\approx 5\times 10^{15}$ cm^2 [29] as the dominant contribution to the neutral-ion relaxation.) The time scale of this process (0.1 ns) is well below the discharge time, i.e., one can consider a steady-state balance between the acceleration in the electric field and collisional de-acceleration, resulting in an average kinetic energy gain of 0.05–0.1 eV per ion. Therefore, for the Stark broadening calculations $T_i = 0.1$ eV was assumed.

TABLE I. Instrumental, resonance, VdW, and Doppler broadening FWHMs of the He I transitions used for diagnostics. Also given are the total Lorentzian (L^{tot}) widths. All values are in units of cm^{-1}. The calculations were performed assuming $n_n = 2\times 10^{19}$ cm^{-3} and $T_n = 0.03$ eV (see the text).

Transition	λ (nm)	Instr.	Resonance	VdW	Doppler	L^{tot}
$2s(^3S)$–$3p(^3P)$	388.86	4.0	0	0.52	0.16	0.52
$2p(^3P)$–$5d(^3D)$	402.62	3.7	0	1.26	0.15	1.26
$2s(^3P)$–$4d(^3D)$	447.15	2.8	0	0.84	0.14	0.84
$2p(^1P)$–$3p(^1D)$	492.20	2.1	1.68	0.84	0.12	2.52
$2p(^1S)$–$3p(^1P)$	501.57	2.0	0.41	0.53	0.12	0.94
$2p(^3P)$–$3d(^3D)$	587.56	1.3	0	0.45	0.10	0.45
$2p(^1P)$–$3d(^1D)$	667.81	1.5	1.68	0.44	0.09	2.12

An example of line-shape analysis is given in Fig. 4, where the experimental data of the triplet $2p$-$4d$ line averaged over a time of 1–2 ns are presented, together with the calculated spectra under different assumptions. The best fit for the F-A separation and F/A ratio is obtained at $n_e \approx 7\times 10^{15}$ cm^{-3} and an optical depth of 2.4. However, as seen from the figure, this line shape strongly overestimates the measured line wings; in addition, the dip between the allowed and forbidden components is too shallow. The source of the extraneous broadening is electrons: In order to fit the line wings, a significantly lower ($n_e = 4\times 10^{15}$ cm^{-3}) density is required; however, the F-A separation is evidently too small in this case. The F-A separation is mainly determined by the slow (ionic) component of the plasma micro field, therefore, one needs to

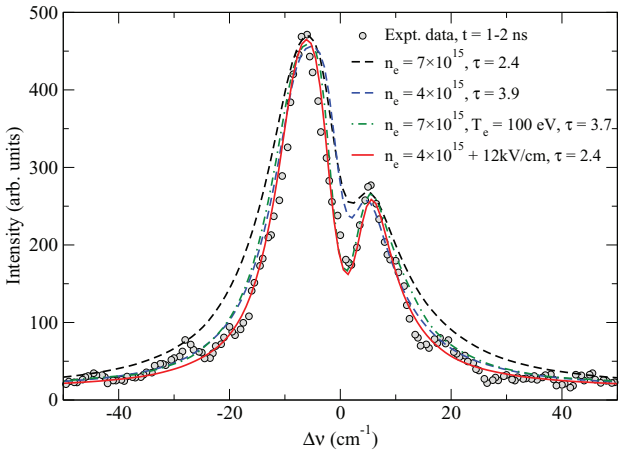

FIG. 4. (Color online) An example of the He I triplet $2p-4d,4f$ data analysis. The experimental data are averaged over $t = 1-2$ ns. The plasma parameters used for the calculations are indicated in the legend. Unless explicitly mentioned $T_e = 2$ eV, $T_i = 0.1$ eV and $T_n = 0.03$ eV was assumed (see the text).

[1]Evidently, this assumes the electrons are kept at a constant temperature by an external mechanism.

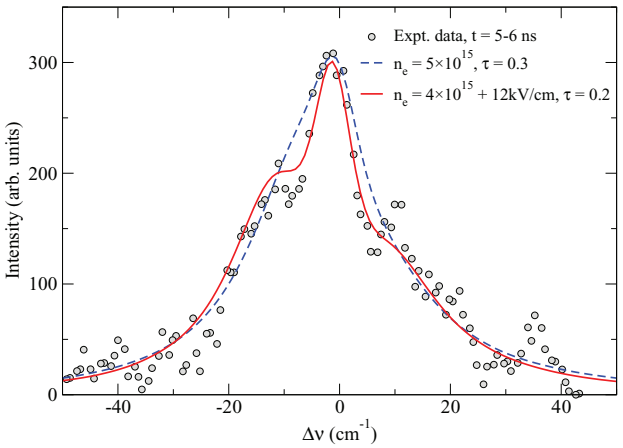

FIG. 5. (Color online) An example of the He I triplet 2p-5d, 5f, 5g data analysis. The experimental data are averaged over $t = 5 - 6$ ns. $T_e = 2$ eV, $T_i = 0.1$ eV and $T_n = 0.03$ eV were assumed for the line shape calculations, with other parameters indicated in the legend.

keep the magnitude of this component while diminishing the electron broadening.

One possibility of achieving this is to significantly increase the electron temperature since the electron broadening decreases with T_e, reaching, for sufficiently high T_e, the impact-limit $\sim 1/\sqrt{T_e}$ asymptote [19]. Indeed, assuming nonequilibrium plasma with T_e =100 eV gives a fairly good fit to the measured spectrum. (We note that simultaneously increasing T_i and/or T_n would result in a complete smearing of the entire allowed-plus-forbidden line structure, due to the ion dynamics). The other possibility is addition of a DC or low-frequency ($\lesssim$10 GHz) electric field.[2] Indeed, assuming such a field with a root-mean-square (RMS) magnitude of $\sim$10 kV/cm allows one to achieve a good fit.

The same analysis was carried out for the singlet $2p$-$4d$ (492 nm) data, resulting in similar conclusions. In addition, we also analyzed the triplet $2p$-$5d$ (402 nm) transition. Due to the higher principal quantum number of the upper states, the energy separations between the $5l$ levels are smaller, while the Stark mixings are larger, than those of the $4l$ levels. As a result, for the plasma densities relevant for this study, the $5d$, $5f$, and 5g states strongly intermix, with the total line shape lacking the clearly identifiable F-A signature of the $2p$-$4d$ transitions.[3] Furthermore, the intensity of this line is rather weak, with a worse SNR of its measured line shapes. Nevertheless, the line-shape analysis of these data also disfavors the simple model of an LTE plasma, suggesting, similar to the $2p$-$4d$ singlet and triplet data, the presence of a low-frequency electric macro field. Examples of the calculations are shown in Fig. 5.

Although the line-shape analysis does not allow for discriminating between the two possibilities ($T_e \gg 10$ eV and a $\sim$10 kV/cm low-frequency or DC electric field), the first one can be ruled out based on the plasma kinetics considerations. To this end, we performed calculations based on

[2]The electric fields having too high frequency would result, not unlike the ion dynamical effect, in additional line broadening.

[3]In addition to these levels, the triplet $5s$ and $5p$ levels were also included in the Hamiltonian for these calculations.

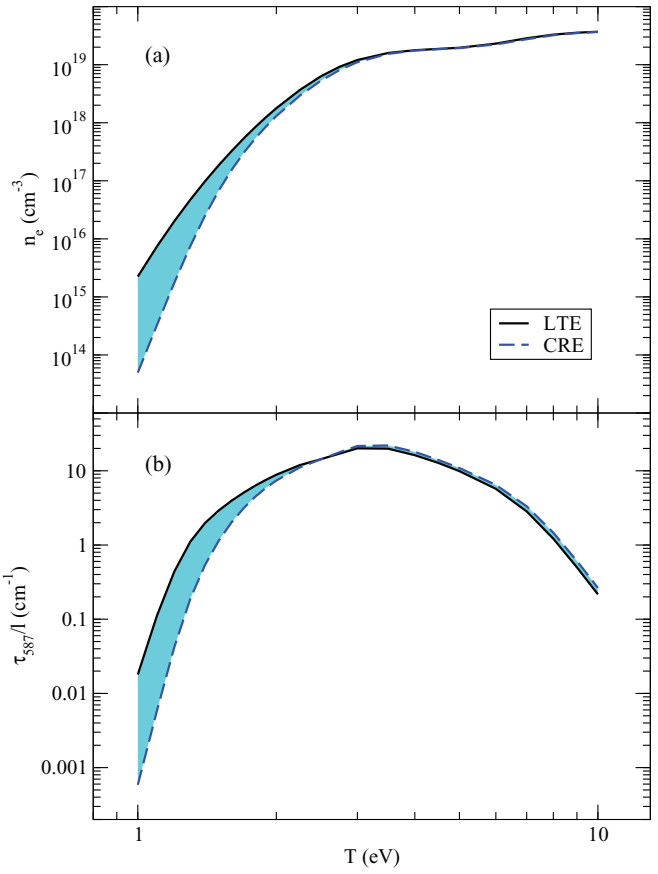

FIG. 6. (Color online) Results of C-R calculations obtained under two stationary conditions: LTE and optically-thin CRE He plasma. In both cases, a constant mass density of 0.18 mg/cm^3 of He gas was assumed. (a) electron density; (b) peak opacity of the 587 nm line per unit length.

the collisional-radiative (C-R) model described in Ref. [30], assuming a plasma mass density of 0.18 mg/cm^3, which corresponds to He gas at $P = 10^5$ Pa at room temperature. Two limiting cases were considered: local thermodynamical equilibrium (LTE) and collisional-radiative equilibrium (CRE) for optically-thin plasma. The results are presented in Fig. 6(a), where the plasma electron density versus the plasma temperature is shown. Evidently, results for a realistic steady-state plasma must lie in the area between these two curves. Therefore, in order to satisfy plasma densities inferred from the Stark analysis, the temperature of a steady-state plasma should be in the range of $1 < T_e < 3$ eV. The rather low temperature of the plasma is further confirmed by the absence of the strong 468.56 nm He II spectral line in the observed spectrum. As the C-R calculations show (Fig. 7), this line should be prominently seen for $T_e \geqslant 3.5$ eV. We note that the much weaker nearby He I 471.31 nm line was observed. Thus, we conclude that the presence of a low-frequency $\sim$10 kV/cm electric field is very likely, while the hypothesis of the plasma having $T_e \gg 10$ eV is unjustified. (It should be stressed, however, that this conclusion is related to the bulk of plasma electrons; a minor fraction of electrons may be very energetic.)

The resultant inferred time histories of the electron density n_e are shown in Fig. 8(a). An electron temperature $T_e = 2$ eV was assumed; however, as was mentioned above, the results

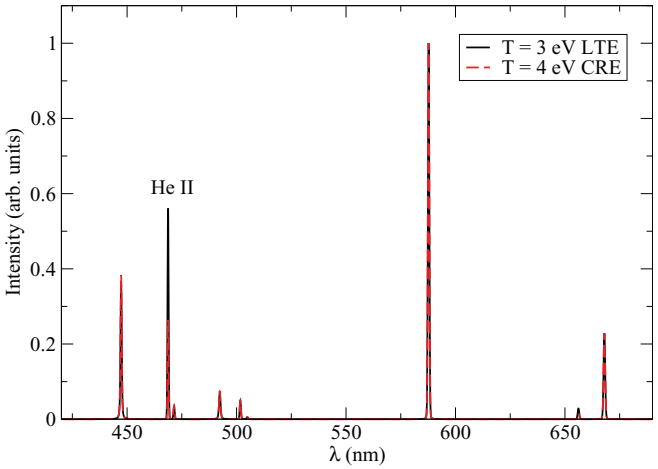

FIG. 7. (Color online) C-R calculations of the visible spectrum of the 3 eV LTE and optically thin 4 eV CRE He plasmas with $n_e = 10^{16}$ cm^{-3}. The spectra are peak-normalized. For the sake of clarity, the spectral lines are assigned fictitious equal widths.

are largely insensitive to the electron temperature: e.g., the differences between the inferred values of n_e assuming $T_e =$ 1 eV and 4 eV are less than 10%. It is seen that the time histories of n_e, as inferred from the analysis of three spectral lines, are in reasonable agreement [see Fig. 8(a)], with the average density $\sim 5 \times 10^{15}$ cm^{-3} and a tendency to slightly increase over time. In contrast to the moderate change of the plasma density, the intensities of the three lines show significantly more pronounced dynamics, changing by almost an order of magnitude during the same time. We note that the relative (normalized to the values at the beginning of the observation) intensities of the lines, shown in Fig. 8(b), are corrected for the opacity according to Eq. (1) and are, therefore, equal to the relative changes of the populations of the upper levels ($4d^3D$, $4d^1D$, and $5d^3D$ for the 447, 492, and 402 nm lines, respectively). The fast asynchronous changes of closely spaced levels (the energies of the $4d^3D$ and $4d^1D$ levels differ by less than 1 meV) strongly indicate a highly transient and nonequilibrium character of the plasma studied.

We note that the inferred opacities of different spectral lines are consistent. The optical depth is proportional to the population of the lower level, the absorption oscillator strength f, and the plasma depth along the line of sight, and inversely proportional to the thin-plasma-limit line width ω (in the energy units). Thus, if two lines share the same lower level and are emitted from the same plasma volume, one should expect

$$\frac{\tau_1}{\tau_2} \approx \frac{f_1}{f_2}\frac{\omega_2}{\omega_1} \tag{9}$$

(the equality is approximate because the line shapes of the two lines are, in general, different; if both are, e.g., Gaussians, the expression becomes exact). This is the case for the $2p$-$4d$ (447 nm) and $2p$-$5d$ (402 nm) triplets. Approximating the width by the dominant Stark broadening and using the Stark FWHM at $n_e = 5 \times 10^{15}$ cm^{-3}, one obtains

$$\frac{\tau_{402\,\mathrm{nm}}}{\tau_{447\,\mathrm{nm}}} \approx 0.12. \tag{10}$$

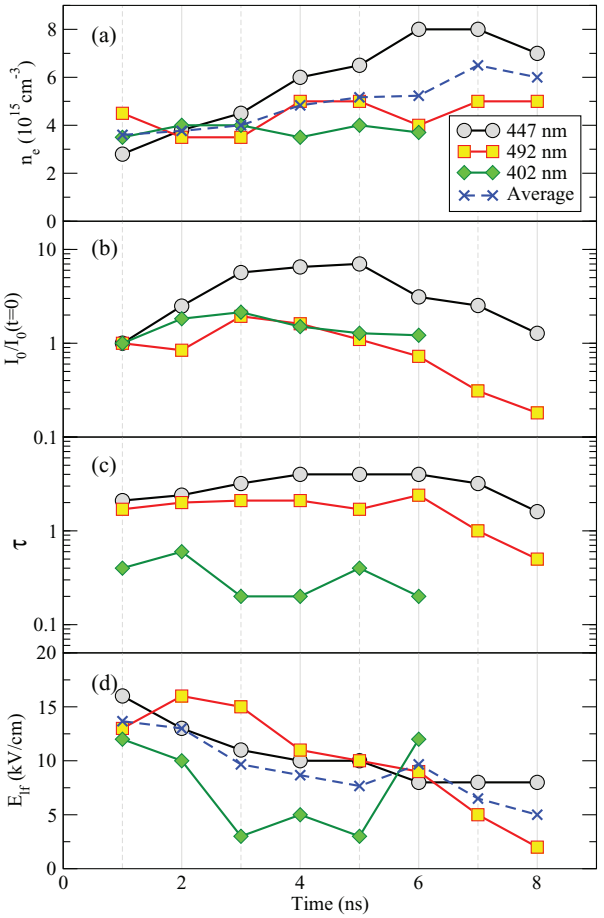

FIG. 8. (Color online) Time evolutions of the plasma electron density (a), relative line intensities (b), peak line opacities (c), and low-frequency electric field (d), inferred from the time-resolved measurements of the He I $2p$-$4d$ triplet (447 nm), $2p$-$4d$ singlet (492 nm), and triplet $2p$-$5d$ (402 nm) line shapes.

This value is in a good qualitative agreement with the inferred data [see Fig. 5(c)], further confirming validity of our data analysis.

Finally, in Fig. 8(d) we plot the low-frequency electric field E_{lf}. We note that the slight decrease of the electric field corresponds to the respective increase of n_e.

For the plasma parameters of interest here, the Stark broadening of all $n = 2$ to $n = 3$ He I transitions is well described by the impact approximation, with the Lorentzian line shape and its width proportional to n_e. Our calculations of the proportionality coefficients, which are rather weakly dependent on T_e, agree within 5%–10% with the previously tabulated ones [19]. We can now apply Eq. (9) to derive time-dependent opacities of the $2p$-$3d$ singlet (667 nm) and triplet (587 nm) transitions based on those of the singlet (492 nm) and triplet (447 nm) transitions [shown in Fig. 6(c)], respectively. Evidently, the Stark broadening of the $2p$-$3d$ line is smaller while the oscillator strength is stronger than those of its $2p$-$4d$ counterpart. As a result, the inferred values of τ of the 587 and 667 nm lines are of the order of 100. It is important to note that these values of peak line opacity can be considered as a strong indication of the nonstationary plasma state. Indeed, our C-R calculations show that even the opacity

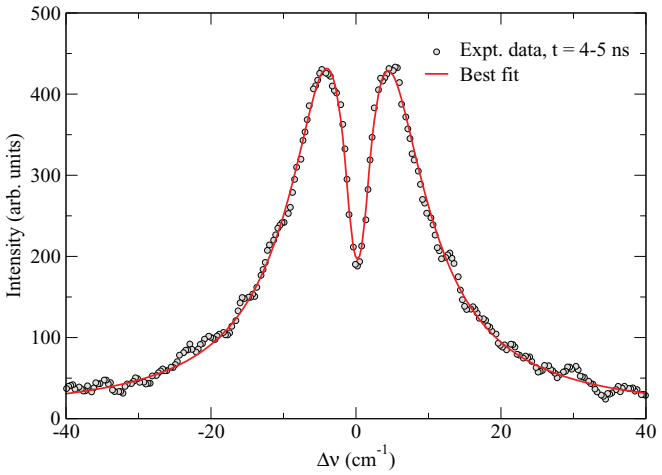

FIG. 9. (Color online) An example of the He I triplet $2p$-$3d$ (587 nm) data analysis. The experimental data are averaged over $t = 4$–5 ns. The best fit made according to Eq. (11) corresponds to $n_{e,2} \approx 2.5 \times 10^{16}$ cm^{-3} of the outer layer.

of the strongest, triplet $2p$-$3d$ (587 nm) line [see Fig. 6(b)] should not exceed ∼1 for either LTE or CRE plasma with $n_e \sim 10^{16}$ cm^{-3} and size ∼1 cm along the line of sight. This value is two orders of magnitude smaller than the opacity inferred from the preceding data analysis.

Huge optical depths for the 587 and 667 nm lines make measurements of the plasma density using these lines impractical. However, this could be turned to advantage for studying plasma regions beyond the main radiating bulk. Indeed, radiation from even a tiny amount of a more dense but moderately opaque plasma would dominate the shape (except perhaps for very far line wings) of these lines. To account for the observed self-reversal of these lines [Fig. 2(d)], we employed a simplified two-layer plasma model, in which the first (inner) layer emits and absorbs the light, while the second (outer) layer only absorbs it:

$$I(\omega) \sim \tau_1^{-1}\{1 - \exp[-\tau_1 L(\gamma_1, d_1; \omega)]\} \times \exp[-\tau_2 L(\gamma_2, d_2; \omega)], \quad (11)$$

where

$$L(\gamma, d; \omega) = \frac{\gamma^2}{(\omega - d)^2 + \gamma^2} \quad (12)$$

is the peak-normalized shifted Lorentzian line profile. For simplicity, the thermal Doppler effect and the instrumental broadening were neglected because of their minor contributions. Based on the Stark calculations, the best-fit γ_1 and γ_2 give n_e of the inner and outer layers, respectively. An example of such a fit is presented in Fig. 9.

As expected, the opacity τ_1 of the inner layer is of the order of few tens for the both 587 and 667 nm lines. Due to the significant opacity of the inner layer, ω_1 and hence $n_{e,1}$ have very large uncertainties; however, $n_{e,2}$ can be inferred with a reasonable accuracy. As seen in Fig. 10(a), both $2p$-$3d$ lines give qualitatively similar values of the plasma density, with the average one around ∼2.5×10^{16} cm^{-3} which is almost constant over time. In order to infer the plasma density in the inner layer $n_{e,1}$, we use the relative shift $d_{02} - d_{01}$ between

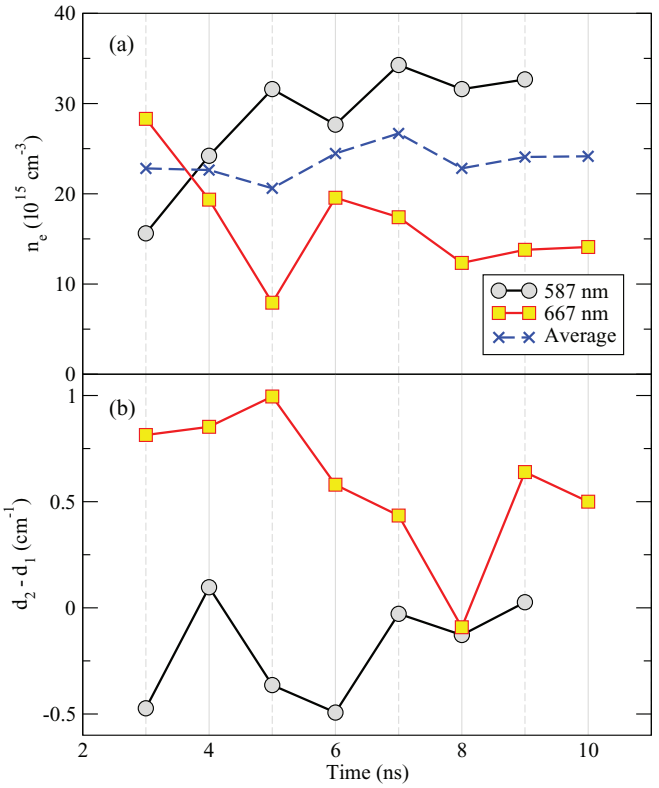

FIG. 10. (Color online) Time evolutions of the plasma electron density (a) and relative line shifts (b), inferred from the time-resolved measurements of the He I $2p$-$3d$ triplet (587 nm) and $2p$-$3d$ singlet (667 nm) line shapes.

the line shapes of the first and second layers, shown in Fig. 10(b). In general, this shift can be due to the different densities and temperatures (resulting in the Stark shift),[4] or bulk velocities (resulting in the Doppler shift) of the two layers, or a combination of these two factors. The rather significant variation with time of the shifts is likely an artifact due to very small values of the shift ($\leqslant$ the pixel size). However, as seen from Fig. 10(b), the relative shifts of the 587 and 667 nm lines have opposite signs, which rules out the Doppler effect. One can see that the relative shift of the 667 nm line is 2–3 times larger than that of the 587 nm line, close to the expected Stark shift ratios of the lines. From our calculations, at $T_e = 2$ eV we obtain $d_{667nm}/d_{587} \approx -1.8$. If we assume equal temperatures of 2 eV of the both layers, the measured relative shifts correspond to $n_{e,1} - n_{e,2} \approx 10^{16}$ cm^{-3}.

C. Spectral lines at $d_C = 1$ mm

Spectral line profiles near the cathode edge show qualitatively similar behavior to the spectral line obtained at $d_C = 5$ mm. However, in a minority of the generator shots an "anomalous" line broadening was observed. Namely, in these shots all spectral lines at $t_L > 4$ ns have an "anomalously broadened" region, as shown in Fig. 11. At later times ($t_L > 10$ ns) the broadened segment remains while the rest

[4]In contrast to the widths, the Stark shifts of these lines have a more pronounced dependence on the plasma temperature.

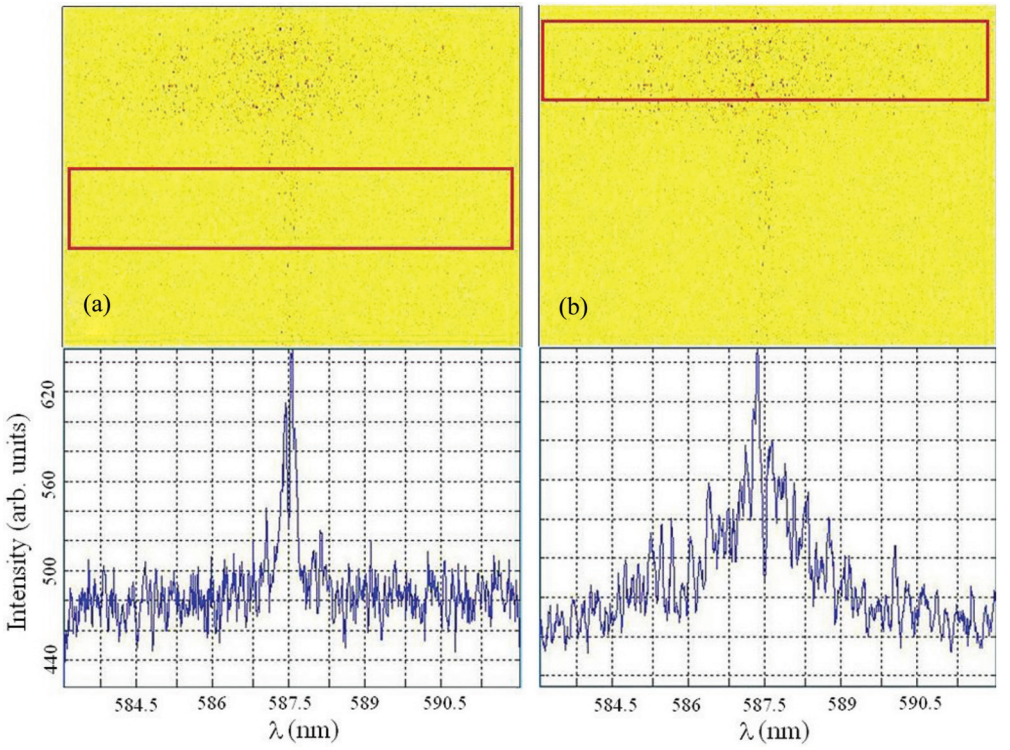

FIG. 11. (Color online) Anomalous broadening of the 587.56 nm spectral line at $t_L = 6.3$ ns. (a) The normal line segment is highlighted with a red rectangle at the top of the image and the corresponding line profile is shown at the bottom. (b) The anomalous broadened segment is highlighted with a red rectangle and the corresponding spectral line profile is shown at the bottom.

of the spectral line is no longer detectable. The time of the appearance of the anomalousregions was rather random, i.e., the line-width's evolution cannot be traced chronologically. In most anomalous shots the spectral line profile representing the broadened segment could not be fitted with a Voight profile. In the shots in which it could be fitted, densities calculated according to the Stark broadening yield values of $\sim 10^{18}$–10^{19} cm^{-3} [19]. The latter can be related to the appearance of bright and "hot" spots on the edge of the cathode [16]. Such a hot spot is apparently a very dense and hot plasma region emitting very broad spectral lines, and this spot remains for long times.

V. DISCUSSION

From the spectral line analysis one infers two distinctive groups of lines representing two significantly different values of the electron density. Namely, spectral lines of the singlet and triplet transitions $2p$-$4d$ (492 nm) and (447.15 nm) and the triplet transition $2p$-$5d$ (402 nm) are emitted from the plasma with density 5×10^{15} cm^{-3} (which henceforth will be referred to as a low-density region), and lines of the singlet and triplet transitions $2s$-$3p$ (388 and 501 nm) and $2p$-$3d$ (587 and 667 nm) are emitted from the plasma with density 3×10^{16} cm^{-3} (which henceforth will be referred as a high-density region); see Table II.

Before we start discussing these results, let us recall the main findings from Ref. [16]. In that study the same experimental setup for gas discharge was used. In the first stage of the discharge ($t < 1$ ns with respect to appearance of light emitting plasma on the edge of the cathode) the emission from the plasma and, respectively, plasma formation, appears on the top and bottom edges of the cathode and its vicinity due to the electric field enhancement at these locations. In majority of the shots, a dominant discharge streamer is formed on the top and/or bottom edge and propagates towards the anode, bridging the gap $d_{CA} = 2$ cm within $\sim$1–1.5 ns with respect to the beginning of the discharge current. After $\sim$1.5 ns, the high-voltage pulse is not terminated in spite of the C-A gap being filled with a light emitting plasma. The latter indicates a high resistance of this plasma. Further development of the gas discharge is governed by the appearance of explosive emission centers in the form of "hot" bright cathode spots at random locations along the cathode edge. These spots serve as origins for new bright discharge channels extending towards the anode and bridging the C-A gap within $\leqslant 2$ ns. These new channels also do not short-circuit the C-A gap and, consequently do not terminate the high-voltage stage of the discharge. Also, it was observed in a single 1 ns frame that two channels can coexist

TABLE II. Summary of the analysis of the spectral lines.

Plasma	λ (nm)	Transition	State
High density plasma	501.57	$2s$-$3p$	triplet
$\sim 3 \times 10^{16}$cm^{-3}	388.86	$2s$-$3p$	singlet
	587.56	$2p$-$3d$	triplet
	667.81	$2p$-$3d$	singlet
Low density plasma	402.62	$2p$-$5d$	triplet
$\sim 5 \times 10^{15}$cm^{-3}	447.15	$2p$-$4d$	triplet
	492.2	$2p$-$4d$	singlet

simultaneously, with one channel extending all the way from the cathode to the anode and the other channel extending to only ∼30% of the C-A gap length. The conclusion is that these channels consist of resistive plasma with lifetime $\leqslant 2$ ns.

Now let us discuss the results of the present spectroscopic research of the parameters of the discharge plasma which strongly indicates an existence of two regions with different electron densities. Whatever the explanation for the presence of two different density regions is, the main question is why all the $n = 4 \rightarrow n = 2$ transitions show no signs of plasma with density greater than 10^{16} cm^{-3}. This question also can be formulated as why the $n = 4$ energy levels appear to be populated in the 5×10^{15} cm^{-3} plasma and not in the 3×10^{16} cm^{-3} plasma, while the $n = 3$ energy levels are populated in the 3×10^{16} cm^{-3} plasma.

A possible reason for population of the excited levels may be nonthermal electrons present in the plasma. These electrons should have a sufficient energy to excite $n = 4$ and $n = 5$ levels, and the duration of this electron flux has to be short enough in order not to allow significant ionization of He I atoms resulting in the appearance of He II ion lines, which were not observed in the experiment. Since the excitation energies of He I and He II are similar, electrons sufficiently energetic to excite He I will also excite He II. The influence of nonthermal electrons on the population dynamics of different atomic levels was checked using C-R simulations. In these simulations, an initial CRE of neutral He atoms, with a density of 2×10^{19} cm^{-3} at $T = 1$ eV that resulted in the plasma electron density $n_e \approx 5 \times 10^{13}$ cm^{-3}, was assumed. At $t = 1$ ns, a nonthermal electron beam with density $n_b = 3 \times 10^{14}$ cm^{-3}, $T_b = 50$ eV electron temperature, and duration of 1 ns was "switched on." The dynamics of population of He I $n = 2$, 3, and 4 levels is shown in Fig. 12. One can see that when the electron beam is switched on, the plasma density increases up to $\sim 2.5 \times 10^{16}$ cm^{-3} within 1 ns, with further "slow" increase up to $\sim 3.5 \times 10^{16}$ cm^{-3}. Another important result is that the energy levels with higher n reach their peak population earlier with respect to the onset of the electron beam. Therefore, the levels with higher n have maximum population in the plasma with lower electron density, e.g., the peak populations of the $n = 4$ levels are reached in the beginning of the electron beam when $n_e \approx 5 \times 10^{15}$ cm^{-3}. In addition, one can see that, for the same value of n, triplet energy states are populated and decaying slower than the respective singlet states, and these differences are more strongly pronounced for lower n values. Indeed, this qualitatively agrees with the experimental results, showing that the triplet $2p$-$4d$ and $2p$-$3d$ transitions "see" higher n_e than their singlet counterparts [see Figs. 8(a) and 10(a)].

Let us now consider a possible reason for the appearance of a short outburst of energetic electrons with a duration of 1–2 ns. The results of the recent research [16] showed existence of several resistive plasma channels in the CA gap with a lifetime of ∼2 ns. The evanescence of a channel is followed by generation of a new channel from a different emission center on the cathode shortly before or after the first channel ceases to exist. Due to a high resistivity of these channels, there appears a radial electric field similar to the case of exploding wires in vacuum [31]. This radial electric field could be responsible for acceleration of plasma electrons in the radial direction leading

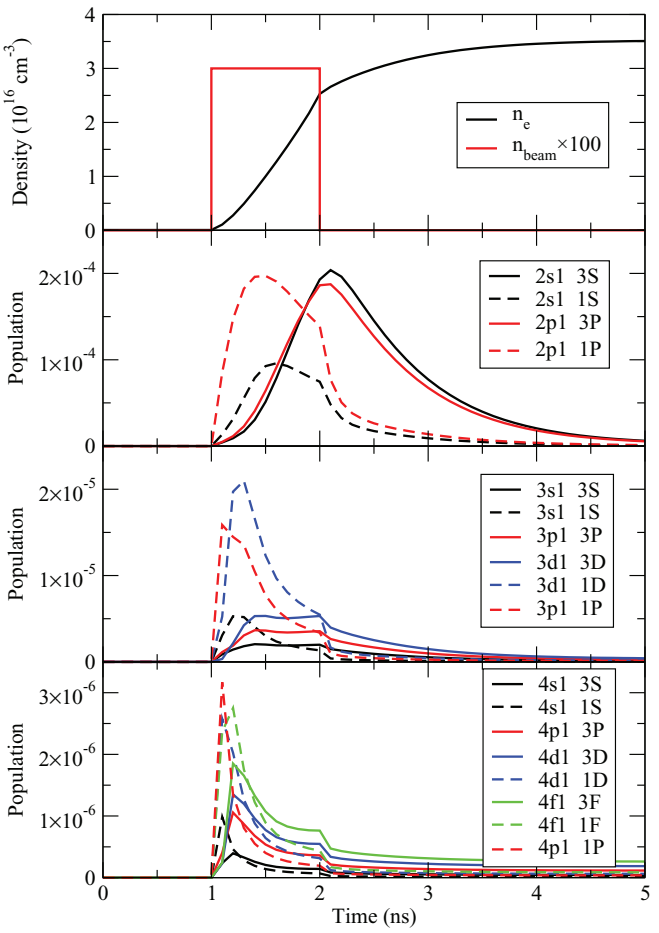

FIG. 12. (Color online) Time evolution of atmospheric pressure non-LTE He plasma. (a) electron density (b)–(d) relative level populations of He I. Electron beam with temperature $T = 50$ eV is acting during 1 ns starting from $t = 1$ ns. Here we assumed density of He atoms $n_{He} \approx 2 \times 10^{19}$ cm^{-3} at temperature $T = 1$ eV.

to formation of the low-density plasma region with highly populated $n \geqslant 4$ He I energy levels.

An additional source of such a radial electric field could be electrons injected into already existing resistive plasma channels from the explosive emission plasma formed at the edge of the cathode. The injection of electrons into a plasma channel leads to fast radial ejection of plasma electrons from the channel due to appearance of a radial electric field [32]. A qualitative presentation of the discharge plasma formation with low outer and higher inner plasma densities is shown in Fig. 13.

One can assume that these energetic electrons, accelerated in the radial direction, form a wave that causes the previously described population dynamics. This wave advances in the radial direction through the low-density plasma and populates excited levels of He I atoms. In the wake of the wave front, the plasma density continues to grow to $\sim 3 \times 10^{16}$ cm^{-3}, but the population of energy levels with $n \geqslant 4$ decreases (see Fig. 12). Thus, one obtains a wave in the form of a cylindrical shell creating the "low-density" plasma that predominantly emits the 447.15, 492.20, and 402.62 nm photons. In the wake of the wave, the bulk plasma channel builds up with an increasing density, due to the discharge current. This dense plasma has

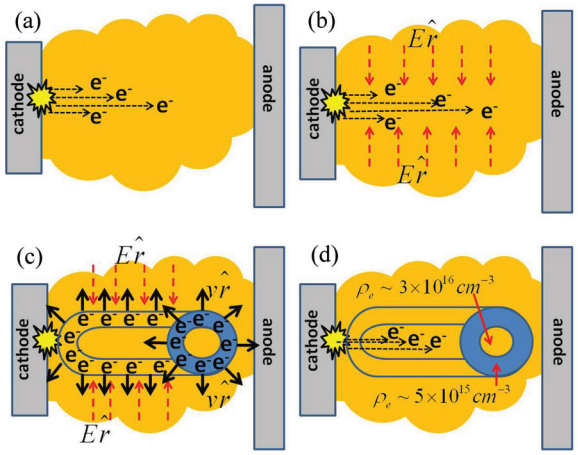

FIG. 13. (Color online) Development of a single channel structure: (a) fast energetic electrons are injected from an explosive emission center on the cathode edge into the gap filled with a low density, resistive plasma; (b) space charge of the injected electrons creates a radial electric field towards the "channel's axis"; (c) radial electric field accelerates plasma electrons in the radial direction generating an excitation wave in a form of cylindrical shell, (d) radial wave of electrons populates the $n \geqslant 4$ levels in plasma with density $n_e \approx 5 \times 10^{15}$ cm^{-3}, behind the wave front a bulk of denser plasma ($n_e \approx 3 \times 10^{16}$ cm^{-3}) produced.

lower populations of the $n \geqslant 4$ levels and predominantly emits photons from the $n = 3$ levels, including 587.56 and 667.81 nm. These photons undergo self-absorption further away from the axis. In spite of the absorption, the intensities of these lines are comparable to those of the 447.15 and 492.2 nm lines, apparently due to relatively large volume of the bulk. The 388.86 nm ($3p$-$2s$ singlet transition) and 501.56 nm ($3p$-$2s$ triplet transition) photons are emitted from the bulk plasma and are absorbed as well, but do not exhibit strong self-reversal due to the lower absorption oscillator strengths of these lines. The lifetime of such an excitation wave should not exceed 1–2 ns in order to avoid populating excited He II levels. This duration is consistent with the lifetime of the hot spots, whose depletion terminates the radial electric field and, therefore, terminates the radial wave of electrons. However, on the same time scale other explosive centers form somewhere else on the cathode edge, followed by a similar development of the discharge channel [16].

VI. SUMMARY

Time- and space-resolved spectroscopy study shows that the plasma formation in a nanosecond electrical discharge in He gas at atmospheric pressure is characterized by formation of discharge channels with nonuniform electron density distribution, namely a dense $\sim 3 \times 10^{16}$ cm^{-3} inner and a low-density outer $\sim 5 \times 10^{15}$ cm^{-3} plasma layer. The electron temperature of these layers was found to be $\sim$2 eV. In order to be consistent with the spectroscopic data, the lifetime of these discharge channels should not exceed 2 ns, which agrees with the an earlier study [16]. Also, the obtained spectroscopic data and analysis strongly indicates an existence of short-duration, radial flux of nonthermal energetic ($>$10 eV) electrons ejected outwards from the main discharge channel and a presence of a quasistatic $\sim$10–20 kV/cm electric filed. Finally, a qualitative model explaining the evolution of the plasma formation was suggested. The model fits the experimental data from both fast-framing photography [16] and optical emission spectroscopy. Nevertheless, further research is required in order to improve the reliability of this qualitative model.

ACKNOWLEDGMENTS

The work of E.S. was partially supported by the Israel Science Foundation. We would like to thank to M. Á. González, Yu. Ralchenko and Q. Xiong for helpful discussions.

[1] P. Babich and T. V. Loiko, Plasma Phys. Rep. **36**, 263 (2010).
[2] V. F. Tarasenko and S. I. Yakovlenko, Plasma Devices Oper. **13**, 231 (2005).
[3] G. A. Mesyats, M. I. Yalandin, A. G. Reutova, K. A. Sharypovb, V. G. Shpakb, and S. A. Shunailov, Plasma Phys. Rep. **38**, 29 (2012).
[4] V. F. Tarasenko, Plasma Phys. Rep. **37**, 444 (2011).
[5] D. Levko, S. Yatom, V. Vekselman, J. Z. Gleizer, V. Tz. Gurovich, and Ya. E. Krasik, J. Appl. Phys. **111**, 013303 (2012).
[6] V. A. Shklyaev and V. V. Ryzhov, Tech. Phys. Lett. **37**, 72 (2011).
[7] T. Shao, C. Zhang, Z. Niu, V. F. Tarasenko, E. Kh. Baksht, A. G. Burahenko, and Y. V. Shut'ko, Appl. Phys. Lett. **98**, 021503 (2011).
[8] H. G. Krompholz, L. L. Hatfield, A. A. Neuber, K. P. Kohl, J. E. Chaparro, and H. Ryu, IEEE Trans. Plasma Sci. **34**, 927 (2006).
[9] S. Yatom, V. Vekselman, J. Z. Gleizer, and Ya. E. Krasik, J. Appl. Phys. **109**, 073312 (2011).
[10] S. Yatom, J. Z. Gleizer, D. Levko, V. Vekselman, V. Gurovich, E. Hupf, Y. Hadas, and Ya. E. Krasik, Europhys. Lett. **96**, 65001 (2011).
[11] S. Yatom, D. Levko, J. Z. Gleizer, V. Vekselman, and Ya. E. Krasik, Appl. Phys. Lett. **100**, 024101 (2012).
[12] A. V. Gurevich, G. A. Mesyats, K. P. Zybin, M. I. Yalandin, A. G. Reutova, V. G. Shpak, and S. A. Shunailov, Phys. Rev. Lett. **109**, 085002 (2012).
[13] R. M. van der Horst, T. Verreycken, E. M. van Veldhuizen, and P. J. Bruggeman, J. Phys. D: Appl. Phys. **45**, 345201 (2012).
[14] D. A. Sorokin, M. I. Lomaev, and K. Yu. Krivonogova, News Tomsk Polytechnic Univ. **316**, 18 (2010) (in Russian).
[15] Q. Xiong, A. Yu. Nikiforov, M. A. Gonzalez, C. Leys, and X. P. Lu, Plasma Sources Sci. Technol. **22**, 015011 (2013).
[16] S. Yatom, V. Vekselman, and Ya. E. Krasik, Phys. Plasmas **19**, 123507 (2012).
[17] J. Valognes and J. Bardet, J. Quant. Spectrosc. Radiat. Transfer **56**, 855 (1996).
[18] M. Ivković, S. Jovićević, and N. Konjević, Spectrochim. Acta B **59**, 591 (2004).
[19] H. R. Griem, *Spectral Line Broadening by Plasmas* (Academic, New York, 1974).
[20] E. Stambulchik, K. Tsigutkin, and Y. Maron, Europhys. Conf. Abstracts **27A**, 1.58 (2003).

[21] K. Tsigutkin, R. Doron, E. Stambulchik, V. Bernshtam, Y. Maron, A. Fruchtman, and R. J. Commisso, Phys. Rev. E **76**, 046401 (2007).
[22] E. Stambulchik and Y. Maron, J. Quant. Spectrosc. Radiat. Transfer **99**, 730 (2006).
[23] A. Kramida, Yu. Ralchenko, and J. Reader (NIST ASD Team), NIST Atomic Spectra Database (version 5.0) http://physics.nist.gov/asd.
[24] M. A. Gigosos and M. A. González, Astron. Astrophys. **503**, 293 (2009).
[25] N. Lara, M. Á. González, and M. A. Gigosos, Astron. Astrophys. **542**, A75 (2012).
[26] H. R. Griem, *Principles of Plasma Spectroscopy* (Cambridge University Press, Cambridge, 1997).
[27] H. A. Bethe and E. E. Salpeter, *Quantum Mechanics of One- and Two-Electron Atoms* (Dover, Mineola, NY, 2008).
[28] M. Mantina, A. C. Chamberlin, R. Valero, C. J. Cramer, and D. G. Truhlar, J. Phys. Chem. A **113**, 5806 (2009).
[29] Yu P. Raizer, J. E. Allen, and V. I. Kisin, *Gas Discharge Physics* (Springer-Verlag, Berlin, 1991).
[30] Y. V. Ralchenko and Y. Maron, J. Quant. Spectrosc. Radiat. Transfer **71**, 609 (2001).
[31] G. S. Sarkisov, P. V. Sasorov, K. W. Struve, D. H. McDaniel, A. N. Gribov, and G. M. Oleinik, Phys. Rev. E **66**, 046413 (2002).
[32] S. Humphries, *Charged Particle Beams* (John Wiley and Sons, New York, 1990), p. 552.